

# Geomagnetic polar minima do not arise from steady meridional circulation

Hao Cao<sup>a,b,1</sup>, Rakesh K. Yadav<sup>a</sup>, and Jonathan M. Aurnou<sup>c</sup>

<sup>a</sup>Department of Earth and Planetary Sciences, Harvard University, Cambridge, MA 02138; <sup>b</sup>Division of Geological and Planetary Sciences, California Institute of Technology, Pasadena, CA 91125; and <sup>c</sup>Department of Earth, Planetary, and Space Sciences, University of California, Los Angeles, CA 90095

Edited by Peter L. Olson, Johns Hopkins University, Baltimore, MD, and approved September 18, 2018 (received for review October 4, 2017)

**Observations of the Earth's magnetic field have revealed locally pronounced field minima near each pole at the core–mantle boundary (CMB). The existence of the polar magnetic minima has long been attributed to the supposed large-scale overturning circulation of molten metal in the outer core: Fluid upwells within the inner core tangent cylinder toward the poles and then diverges toward lower latitudes when it reaches the CMB, where Coriolis effects sweep the fluid into anticyclonic vortical flows. The diverging near-surface meridional circulation is believed to advectively draw magnetic flux away from the poles, resulting in the low intensity or even reversed polar magnetic fields. However, the interconnections between polar magnetic minima and meridional circulations have not to date been ascertained quantitatively. Here, we quantify the magnetic effects of steady, axisymmetric meridional circulation via numerically solving the axisymmetric magnetohydrodynamic equations for Earth's outer core under the magnetostrophic approximation. Extrapolated to core conditions, our results show that the change in polar magnetic field resulting from steady, large-scale meridional circulations in Earth's outer core is less than 3% of the background field, significantly smaller than the ~100% polar magnetic minima observed at the CMB. This suggests that the geomagnetic polar minima cannot be produced solely by axisymmetric, steady meridional circulations and must depend upon additional tangent cylinder dynamics, likely including nonaxisymmetric, time-varying processes.**

geodynamo | polar magnetic minima | polar vortex | gyroscopic pumping | flow magnetic field interactions

In an era of in situ exploration of planetary bodies in the solar system and remote exploration of planetary bodies outside the solar system, the intrinsic magnetic field of the Earth (1, 2), the best documented of all planetary magnetic fields (3, 4), serves as a key test of our understanding of the planetary dynamo mechanism. A few distinct features stand out in the present-day geomagnetic field when downward extrapolated to the core–mantle boundary (CMB) (Fig. 1) (5). Here we will focus on the region within the so-called tangent cylinder (TC), which is the imaginary cylinder co-axial with the spin axis and tangent to the inner core's equator (Fig. 1C). Within the TC, the radial magnetic field on the CMB features weak and even reversed magnetic flux patches in both hemispheres, commonly referred to as polar magnetic minima (6). The amplitude of the relative axisymmetric polar magnetic minima is defined as

$$\frac{|dB_r|}{B_r^{\max}} = \frac{|B_r^{\text{pole}} - B_r^{\max}|}{|B_r^{\max}|}, \quad [1]$$

where  $B_r^{\max}$  ( $B_r^{\text{pole}}$ ) is the maximum (polar) value of the azimuthally averaged, radial magnetic field on the CMB. The value of  $|dB_r|/|B_r^{\max}|$  is ~100% for the northern hemisphere and ~60% for the southern hemisphere (Fig. 1B).

By tracking the time evolution of the polar magnetic minima and attributing the changes in the magnetic field to steady-state axisymmetric advection by core flows, Olson and Aurnou (12) inferred the existence of an axisymmetric, anticyclonic polar vor-

tex inside the TC near the surface of the outer core with characteristic azimuthal velocity  $u_\phi \sim 0.1$  mm/s. A similar axisymmetric CMB flow field was found via inversion of the high-resolution Ørsted satellite magnetic field data (13) and in subsequent studies using different assumptions and datasets (14, 15). The magnetic Reynolds number associated with the inferred ~0.1 mm/s polar vortex, defined as  $Rm = u_\phi R_C / \eta$ , is ~500, taking the core radius  $R_C = 3485$  km for length scale and  $\eta \sim 0.8$  m<sup>2</sup>/s as the magnetic diffusivity (16, 17). The possibility of such a polar vortex extending axially throughout the TC, and its connection to the seismically inferred inner core superrotation, has been extensively investigated (18–23). TC-filling polar vortices have also been found in a number of geodynamo models (7, 11, 20, 24). Thus, an axisymmetric polar vortex is presently the canonical flow believed to exist within the TC (e.g., figure 1 in ref. 11 and Fig. 1C).

Recent high-resolution geomagnetic field inversions have suggested the possibility of an alternative scenario in which an accelerating nonaxisymmetric jet exists along the TC rim (25). Additionally, seismic observations suggest a shuffling rotation of the Earth's inner core, switching between superrotation and subrotation on a decadal time scale (22), rather than the constant superrotation that would better support the existence of quasi-steady, axisymmetric polar vortices. These studies call into question the leading interpretation of the polar magnetic minima, in which meridional circulation associated with the inferred polar vortices advects magnetic flux away from the poles below the

## Significance

The geomagnetic field provides one of the best diagnostics of Earth's core dynamics. In the polar regions of the core–mantle boundary (CMB), the geomagnetic field features weak and even reversed magnetic fluxes that have been referred to as polar magnetic minima. The origin of the geomagnetic polar minima has been commonly attributed to divergent advection of magnetic fluxes by meridional circulation associated with anticyclonic polar vortices. In this study, we performed a quantitative evaluation of this canonical picture. Our analysis showed that steady meridional circulation associated with observed anticyclonic polar vortices are not capable of creating the observed geomagnetic polar minima. We propose three alternative possibilities for the origin of the geomagnetic polar minima.

Author contributions: H.C. and J.M.A. designed research; H.C. and R.K.Y. performed research; H.C. and R.K.Y. analyzed data; and H.C. and J.M.A. wrote the paper.

The authors declare no conflict of interest.

This article is a PNAS Direct Submission.

Published under the PNAS license.

Data deposition: The snapshots reported in this paper are available in Movie S1 and on Figshare, <https://doi.org/10.6084/m9.figshare.7152665>.

<sup>1</sup>To whom correspondence should be addressed. Email: haocao@fas.harvard.edu.

This article contains supporting information online at [www.pnas.org/lookup/suppl/doi:10.1073/pnas.1717454115/-DCSupplemental](http://www.pnas.org/lookup/suppl/doi:10.1073/pnas.1717454115/-DCSupplemental).

Published online October 16, 2018.

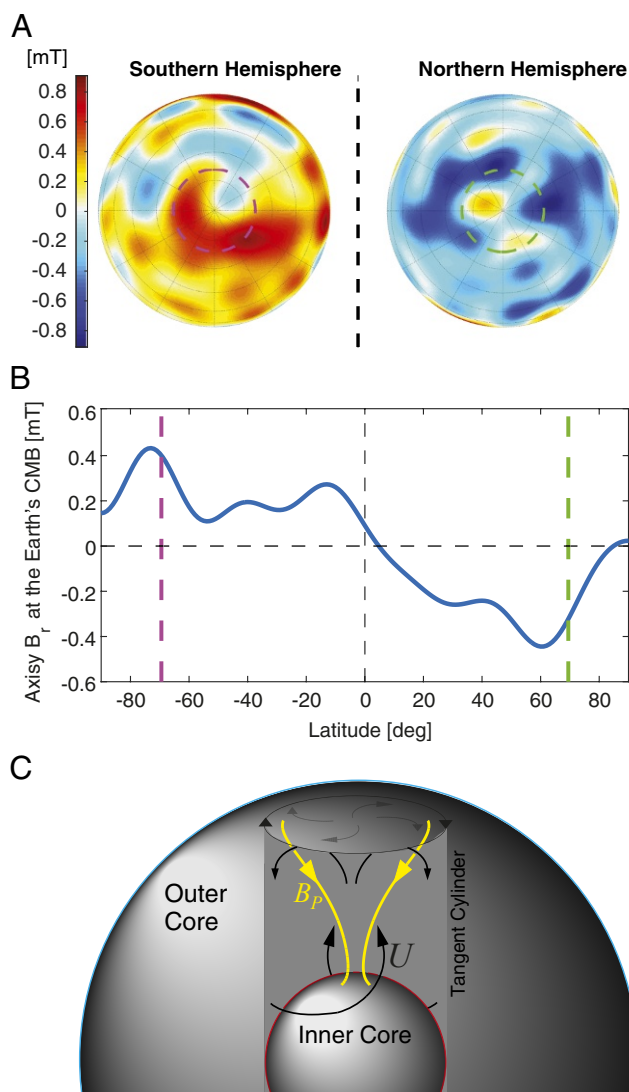


**Fig. 1.** Current epoch geomagnetic field at the Earth’s CMB (5) and the canonical picture of the origin of polar magnetic minima (7–11). (A) The radial component of the geomagnetic field at the CMB (5). The southern hemisphere is shown in *Left*, while the northern hemisphere is shown in *Right*. It can be seen that the region poleward of the TC (pink and green dashed circles) features weak and reserved magnetic flux in both hemispheres. (B) The axisymmetric radial magnetic field at the CMB. The relative amplitude of the axisymmetric polar magnetic minima,  $|dB_r|/|B_r^{\max}|$ , is  $\sim 100\%$  ( $\sim 60\%$ ) in the northern (southern) hemisphere. (C) The leading explanation for the origin of the polar magnetic minima: Meridional circulation associated with the inferred TC polar vortex advects magnetic flux away from the poles. (C) Poloidal magnetic field lines are shown as yellow lines, and velocities are marked by black lines.

CMB (7–11, 26). Furthermore, the essential hypotheses underlying this idea remain untested since neither (i) the amplitude of the meridional circulation associated with the polar vortices nor (ii) the amplitude of the polar magnetic minima associated with the meridional circulation have been quantified. To address this deficit, we determine here under what conditions the meridional circulations associated with steady, axisymmetric polar vortices are capable of generating polar magnetic minima of comparable strength to those observed. Steady, magnetostrophically balanced core flow, which can be convection-driven (e.g., thermal plume) or Lorentz-force-driven, is the focus of this study.

## Ekman Pumping and Gyroscopic Pumping

Before delving into the modeling efforts, we first develop scaling predictions for the strength of polar meridional circulations. In rapidly rotating fluid systems, net transport occurs in the direction perpendicular to both the net body/surface force  $F\hat{f}$  and the spin-axis  $\hat{z}$ , as dictated by the local force balance between  $F\hat{f}$  and the Coriolis forces (e.g., refs. 27–29):

$$2\rho_0\Omega\hat{z}\times\mathbf{u}=F\hat{f}, \quad [2]$$

where  $\rho_0$  is the fluid density,  $\Omega$  is the background rotation rate, and  $\mathbf{u}$  is the fluid transport velocity. For example, a negative zonal force (zonal corresponds to azimuthal) would require flows away from the spin axis in the positive cylindrical radial direction ( $+\hat{s}$ ), while a positive zonal force would require flows toward the spin axis ( $-\hat{s}$ ). Mass conservation necessitates the existence of flows in the vertical direction ( $\pm\hat{z}$ ), giving rise to a global meridional circulation (*SI Appendix, Figs. S2 and S5*).

In the hydrodynamic context of atmospheric and oceanic dynamics, this phenomenon is referred to as Ekman pumping (e.g., refs. 27–29). In systems with stress-free mechanical boundary conditions, Ekman pumping effects generate a net meridional transport  $u_{MC}$  that scales linearly with the Ekman number,  $E$ , the ratio of viscous and Coriolis forces. In contrast, when the boundary conditions are no-slip, boundary layer processes alter the pumping efficiency such that  $u_{MC} \sim E^{1/2}$ .

The generalization of Ekman pumping to magnetohydrodynamic (MHD) systems is called gyroscopic pumping and has been extensively investigated in the context of stellar interior dynamics (e.g., refs. 30 and 31). In gyroscopic pumping, the force that pumps the fluid can be any body force, including Lorentz forces. Here we emphasize that gyroscopic pumping describes a balanced state, rather than specifying the causality between the force and the flows, which is an intricate question for a fully dynamical system (see [SI Appendix](#) for more discussion). The cylindrical radial velocity  $u_s$  associated with the Lorentz force in the zonal direction  $F_{L,\phi}$  is

$$u_s = \frac{F_{L,\phi}}{2\rho_0\Omega}. \quad [3]$$

Under axisymmetry, the Lorentz force becomes

$$F_{L,\phi}^{axi} = \frac{\mathbf{B}_{r,\theta}^{axi} \times (\nabla \times \mathbf{B}_{\phi}^{axi})}{\mu_0}, \quad [4]$$

where  $\mu_0$  is the magnetic permeability and  $\mathbf{B}_{r,\theta}^{axi}$  and  $\mathbf{B}_{\phi}^{axi}$  are the axisymmetric meridional (or poloidal) magnetic field and the axisymmetric zonal (or toroidal) magnetic field, respectively. From here onwards, we consider only axisymmetric quantities and drop all *axi* superscripts. The efficiency of meridional circulation to advect magnetic flux can be assessed via the magnetic Reynolds number

$$Rm_{MC} = \frac{u_s D}{\eta} \sim \frac{1}{2} \sqrt{\Lambda(B_{r,\theta})} \sqrt{\Lambda(B_\phi)}, \quad [5]$$

where  $D$  is the typical length scale and  $\Lambda$  is the Elsasser number

$$\Lambda = \frac{B^2}{\mu_0 \eta \rho_0 \Omega} \quad [6]$$

that estimates the ratio of Lorentz and Coriolis forces and is of order unity on Earth’s CMB (4). Recent low-viscosity numerical dynamo simulations (24, 32, 33) also find Elsasser numbers associated with the internal magnetic field to be between 0.4 and 32, in basic agreement with the  $\Lambda \sim 1$  predictions of asymptotic





(cylindrical) radial flow in our dynamic magnetostrophic models is not limited to the boundary layers at the top and bottom of the outer core but fills the entire outer core (SI Appendix, Figs. S2C and S5C).

Fig. 2 shows the amplitude of the relative polar magnetic minima as a function of the Ekman number from kinematic and dynamic calculations at  $\mathcal{A}_{TW} = 300$  and  $\Lambda_{imp}(\text{uniform } B_z) = 1$ . The meridional circulation in the kinematic surveys comes solely from the viscous Ekman pumping. It can be seen from Fig. 2 that the relative amplitude of polar magnetic minima in the kinematic surveys follows the classical  $E^{1/2}$  scaling in the no-slip cases and the  $E^1$  scaling in the free-slip cases (38). In the no-slip kinematic cases,

$$\frac{|dB_r|}{|B_r^{max}|} = 0.32 Rm(u_\phi) E^{1/2}, \quad [9]$$

while in the free-slip kinematic cases,

$$\frac{|dB_r|}{|B_r^{max}|} = 2.82 Rm(u_\phi) E^1, \quad [10]$$

where the value of the azimuthal magnetic Reynolds number  $Rm(u_\phi)$  is controlled by the thermal forcing (SI Appendix, Fig. S1). Given that  $Rm(u_\phi)$  of the inferred anticyclonic polar vortex at the Earth's outer core is  $\sim 500$  (12, 16, 17) and  $E$  of the Earth's core is  $\sim 1 \times 10^{-15}$ , our kinematic survey predicts the relative polar magnetic minima associated with Ekman pumping to be on the order of  $5 \times 10^{-6}$  for the Earth's core under no-slip boundary conditions. This is many orders of magnitude smaller than the observed  $\sim 100\%$  polar magnetic minima at the Earth's CMB. In contrast, for a modest Ekman number commonly adopted in 3D geodynamo simulations such as  $E = 3 \times 10^{-5}$ , our kinematic survey predicts  $|dB_r|/|B_r^{max}|$  as large as 88% for  $Rm(u_\phi) = 500$  with no-slip boundary conditions and  $\sim 4\%$  with free-slip boundary conditions. The strong  $|dB_r|/|B_r^{max}|$  signatures of viscous Ekman pumping likely then influence the global field strengths and the large-scale field morphologies in moderate Ekman number dynamo studies with no-slip boundary conditions (e.g., refs. 26, 39, and 40). We will return to this point later when examining our own 3D numerical dynamo simulations (32).

In the dynamic surveys with  $\mathcal{A}_{TW} = 300$ ,  $|dB_r|/|B_r^{max}|$  follows a  $E^{1/8}$  scaling in the no-slip cases and a  $E^{1/4}$  scaling in the free-slip cases (Fig. 2). In the no-slip dynamic cases with  $\mathcal{A}_{TW} = 300$ ,

$$\frac{|dB_r|}{|B_r^{max}|} = 1.06 E^{1/8}, \quad [11]$$

while in the free-slip dynamic cases with  $\mathcal{A}_{TW} = 300$ ,

$$\frac{|dB_r|}{|B_r^{max}|} = 2.2 E^{1/4}. \quad [12]$$

We have varied  $\mathcal{A}_{TW}$  from 300 to 6,000 and observed similar, but not constant, scalings with the Ekman number in our dynamic surveys (SI Appendix, Fig. S4). The inclusion of Lorentz forces drives much stronger polar vortical flows in the dynamic calculations, with strong  $z$ -invariant component of the zonal flows (36–38). For example, at  $E = 3 \times 10^{-6}$  and  $\mathcal{A}_{TW} = 600$ , the amplitude of the  $z$ -invariant zonal flow inside the TC exceeds that of the  $z$ -varying zonal flow (thermal wind) in both the free-slip case and the no-slip case (SI Appendix, Figs. S2 and S3). These calculations point to the possibility that a significant fraction of the observed anticyclonic polar vortices at the Earth's outer core could be  $z$ -invariant, which would differ from the results of most 3D numerical geodynamo simulations (24, 26, 41).

Next, we extrapolate our scaling results to Earth's core. We use the dynamic scalings derived from both no-slip cases and free-slip cases. The amplitude of the  $z$ -invariant zonal flows scales as  $E^{-1/2} \int_z F_{Lorentz, \phi} dz$  with no-slip boundary conditions and scales as  $E^{-1} \int_z F_{Lorentz, \phi} dz$  with free-slip boundary conditions (37, 38). Thus, free-slip cases at  $E = 3 \times 10^{-8}$  should serve as a proxy for no-slip cases at  $E = 10^{-15}$ . The amplitude of the polar vortex in the free-slip dynamic calculations at  $E = 3 \times 10^{-6}$ ,  $\mathcal{A}_{TW} = 300$  already exceeds the inferred polar vortex amplitude in Earth's core ( $Rm(u_\phi) \simeq 500$ ). Within the framework of our dynamic magnetostrophic models, we regard  $\mathcal{A}_{TW} = 300$  as an upper bound of thermal forcing for  $Rm(u_\phi) \simeq 500$ . The predicted polar magnetic minima is  $\sim 3\%$  when we extrapolate the  $E^{1/4}$  dynamic free-slip scaling to  $E = 3 \times 10^{-8}$  and  $\sim 1.4\%$  when we extrapolate the  $E^{1/8}$  dynamic no-slip scaling to  $E = 10^{-15}$ . However, even the 3% estimate is more than an order of magnitude smaller than the observed 60–100% polar magnetic minima at the Earth's CMB.

The zonal Lorentz force and the cylindrical radial velocity ( $u_s$ ) in the dynamic free-slip calculations with  $\mathcal{A}_{TW} = 300$ ,  $E = 3 \times 10^{-6}$ ,  $\Lambda_{imp}(\text{uniform } B_z) = 1$  are shown in SI Appendix, Fig. S5. The amplitude of the meridional circulation, as measured by  $Rm(u_s)$ , is indeed on the order of unity as predicted by our simple order of magnitude analysis of the Lorentz-force-driven gyroscopic pumping (Eq. 5). Moreover, SI Appendix, Fig. S5C shows the gradual decrease in the amplitude of the meridional circulation in the dynamic calculations as the Ekman number decreases. This decrease in the amplitude of the meridional circulation results from the decrease of zonal Lorentz force and is responsible for the corresponding scaling of  $|dB_r|/|B_r^{max}|$  with the Ekman number in the dynamic calculations.

The geometry (SI Appendix, Fig. S1) and amplitude of the imposed poloidal magnetic fields have been varied in our numerical experiments. These calculations show that the geometry of the imposed axisymmetric magnetic field does not fundamentally alter the amplitude and scaling of the resulted polar magnetic minima (SI Appendix, Fig. S6). When the amplitude of the imposed field is varied,  $|dB_r|/|B_r^{max}|$  reaches the maximum when the Elsasser number of the imposed poloidal magnetic field is in the range of 1 to 10 in the dynamic calculations, as shown in SI Appendix, Fig. S7. Further, the same  $\sim E^{1/4}$  scaling at  $\mathcal{A}_{TW} = 300$  is found for  $|dB_r|/|B_r^{max}|$  in stress-free dynamic calculations at  $\Lambda_{imp} = 10$ . These results imply then that

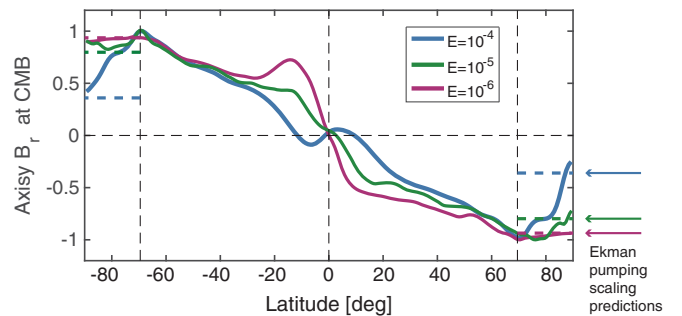


**Fig. 3.** Axisymmetric radial magnetic field at the CMB, scaled to the peak  $B_r$ , from 3D global numerical dynamo simulations with  $Rm(u_\phi, TC) \sim 200$  at three different Ekman numbers:  $10^{-4}$ ,  $10^{-5}$ , and  $10^{-6}$ . For all three Ekman numbers, the polar magnetic minima in the 3D runs are in good agreement with that associated with Ekman pumping predicted by our scaling [9],  $0.32 Rm(u_\phi) E^{1/2}$ , the values of which are shown via the dashed horizontal lines and arrows of the respective colors. For all three Ekman numbers, a random snapshot is chosen that is representative of the entire run (see SI Appendix, Movie S1; also available at <https://doi.org/10.6084/m9.figshare.7152665>).



gratefully acknowledges the support of the National Science Foundation Geophysics Program (Award EAR-1547269). The two higher Ekman number 3D dynamo simulations were carried out at Gesellschaft für wissenschaftliche Datenverarbeitung mbH, Göttingen (GWGD) and at Rechenzentrum Garching der Max-Planck-Gesellschaft (RZG). The lowest Ekman number case was carried out on the ALCF Mira supercomputer (DE-AC02-06CH11357) through the Innovative and Novel Computational Impact on Theory and Experiment (INCITE) program.

number case was carried out on the ALCF Mira supercomputer (DE-AC02-06CH11357) through the Innovative and Novel Computational Impact on Theory and Experiment (INCITE) program.

28. McWilliams JC (2006) *Fundamentals Geophysics Fluid Dynamics* (Cambridge Univ Press, Cambridge, UK).
29. Vallis GK (2006) *Atmospheric and Oceanic Fluid Dynamics* (Cambridge Univ Press, Cambridge, UK).
30. Garaud P, Acevedo Arreguin L (2009) On the penetration of meridional circulation below the solar convection zone. II. Models with convection zone, the Taylor-Proudman constraint, and applications to other stars. *Astrophys J* 704:1–16.
31. Miesch MS, Hindman BW (2011) Gyroscopic pumping in the solar near-surface shear layer. *Astrophys J* 743:79.
32. Yadav RK, Gastine T, Christensen UR, Wolk SJ, Poppenhaeger K (2016) Approaching a realistic force balance in geodynamo simulations. *Proc Natl Acad Sci USA* 113:12065–12070.
33. Aubert J, Gastine T, Fournier A (2017) Spherical convective dynamos in the rapidly rotating asymptotic regime. *J Fluid Mech* 813:558–593.
34. Calkins MA, Julien K, Tobias SM (2017) Inertia-less convectively-driven dynamo models in the limit of low Rossby number and large Prandtl number. *Phys Earth Planet Inter* 266:54–59.
35. Roberts PH (1988) On topographic core-mantle coupling. *Geophys Astrophys Fluid Dyn* 44:181–187.
36. Taylor JB (1963) The magneto-hydrodynamics of a rotating fluid and the earth's dynamo problem. *Proc R Soc Lond Ser A* 274:274–283.
37. Hollerbach R, Ierley GR (1991) A modal  $\alpha^2$ -dynamo in the limit of asymptotically small viscosity. *Geophys Astrophys Fluid Dyn* 56:133–158.
38. Livermore PW, Bailey LM, Hollerbach R (2016) A comparison of no-slip, stress-free and inviscid models of rapidly rotating fluid in a spherical shell. *Sci Rep* 6:22812.
39. Aubert J, Labrosse S, Poitou C (2009) Modelling the palaeo-evolution of the geodynamo. *Geophys J Int* 179:1414–1428.
40. Driscoll PE (2016) Simulating 2 Ga of geodynamo history. *Geophys Res Lett* 43:5680–5687.
41. Aubert J (2005) Steady zonal flows in spherical shell dynamos. *J Fluid Mech* 542:53–67.
42. Calkins MA, Julien K, Tobias SM, Aurnou JM (2015) A multiscale dynamo model driven by quasi-geostrophic convection. *J Fluid Mech* 780:143–166.
43. Ranjan A, Davidson PA (2014) Evolution of a turbulent cloud under rotation. *J Fluid Mech* 756:488–509.
44. Stellmach S, et al. (2014) Approaching the asymptotic regime of rapidly rotating convection: Boundary layers versus interior dynamics. *Phys Rev Lett* 113:254501.
45. Sreenivasan B, Gopinath V (2017) Confinement of rotating convection by a laterally varying magnetic field. *J Fluid Mech* 822:590–616.
46. Sreenivasan B, Jones CA (2006) Azimuthal winds, convection and dynamo action in the polar regions of planetary cores. *Geophys Astrophys Fluid Dyn* 100:319–339.
47. Aubert J, Aurnou J, Wicht J (2008) The magnetic structure of convection-driven numerical dynamos. *Geophys J Int* 172:945–956.
48. Seilamayer M, et al. (2014) Experimental evidence for nonaxisymmetric magnetorotational instability in a rotating liquid metal exposed to an azimuthal magnetic field. *Phys Rev Lett* 113:024505.
49. Gilman P, Dikpati M (2014) Baroclinic instability in the solar tachocline. *Astrophys J* 787:60.
50. Anderson BJ, et al. (2012) Low-degree structure in Mercury's planetary magnetic field. *J Geophys Res* 117:E00L12.
51. Moore KM, et al. (2018) A complex dynamo inferred from the hemispheric dichotomy of Jupiter's magnetic field. *Nature* 561:76–78.
52. Cao H, Russell CT, Wicht J, Christensen UR, Dougherty MK (2012) Saturn's high degree magnetic moments: Evidence for a unique planetary dynamo. *Icarus* 221:388–394.
53. Dougherty MK, et al. (2018) Saturn's magnetic field revealed by the Cassini Grand Finale. *Science* 362:eaat5434.